Design of fin structures for phase change material (PCM) melting process in rectangular cavities

(Article begins on next page)

11 March 2025

| 1 | **DESIGN OF FIN STRUCTURES FOR PHASE CHANGE MATERIAL (PCM) MELTING** |
| 2 | **PROCESS IN RECTANGULAR CAVITIES** |

3

4   **Rejane De Césaro Oliveski [1], Fábio Becker[1], Luiz Alberto Oliveira Rocha [1], Cesare Biserni [2]**
5   **and Gabriel Eduardo Strohm Eberhardt[1]**

6   [1] Mechanical Engineering Graduate Program, Universidade do Vale do Rio dos Sinos, 93022-750 São Leopoldo, Brazil
7   [2] Dipartimento di Ingeneria Industriale, Università degli Studi di Bologna, Viale Risorgimento 2, 40136 Bologna, Italy

8

9   **Abstract**

10   The objective of this work is to analyze the lauric acid PCM melting process in a finned rectangular
11   cavity, keeping both the PCM mass and the total fin area constant, thus changing only the fin aspect
12   ratio. The analysis was conducted through a parametric study of 78 different fin configurations. In
13   order to maintain the thermal capacity, the cavity and fin areas were kept constant while fin
14   dimensions were varied within a preset number of combinations of area fraction and width. The fins
15   tested were combinations of 9 fin aspect ratios (RA_f) and 9 fin-to-cavity area fractions (ϕ). A finite-
16   volume numerical CFD method was used to obtain the results. Governing equations were the
17   conservation of mass, momentum and energy while phase change was governed by an enthalpy-
18   porosity model. The mathematical model was validated against reference experimental results and
19   computational meshes were checked with GCI. For all tested cases, with an increase in the fin length
20   and a consequent reduction in RA_f, there was a reduction of the total time of the melting process. The
21   RA_f, which had shorter melting times, were defined as optimal aspect ratios (RA_{opt}). Thus, each ϕ
22   tested resulted in its own RA_{opt}. For ϕ = 0.005, 0.01, 0.02, 0.03, 0.04, 0.05, 0.1, 0.2 and 0.3, RA_{opt} =
23   0.013, 0.026, 0.052, 0.078, 0.104, 0.130, 0.260, 0.592 and 0.889, respectively. Future works could
24   contemplate a greater number of fins, with the same total area of this study, other PCM and other
25   temperature differences, for example.

26

29   *Nomenclature*

30	A_c	cavity area, $A_c = H\,W$	[m^2]
31	A_f	fin area, $A_f = H_f / W_f$	[m^2]
32	C	porous zone constant	[kg m^{-3} s^{-1}]
33	c_p	specific heat	[J kg^{-1} K^{-1}]
34	Fo	Fourier number, $Fo = \alpha\,t / L_c^2$	[-]
35	$\vec{g}$	gravity	[m s^{-2}]
36	H	cavity height	[mm]
37	h	heat transfer coefficient	[W m^{-2} K]

38	k	thermal conductivity	[W m^{-1} K^{-1}]
39	L	latent heat	[J kg^{-1}]
40	L_c	characteristic length, $\left(L_c = A_c^{1/2}\right)$	[mm]
41	Nu	Nusselt number, $Nu = h\,L_c\,/\,k$	[-]
42	p	pressure	[Pa]
43	q''	heat flux	[W m^{-2}]
44	RA	aspect ratio, $AR = H\,/\,W$	[-]
45	$\vec{S}$	momentum equation source term	[Pa m^{-1}]
46	T	temperature	[K]
47	t	time	[s]
48	$\vec{V}$	velocity vector	[m s^{-1}]
49	W	cavity width	[mm]
50	W_f	fin width	[mm]
51			
52	*Greek symbols*		
53	β	liquid fraction	[-]
54	ε	computational constant	[0,001]
55	λ	specific enthalpy	[J kg^{-1}]
56	μ	dynamic viscosity	[kg m^{-1} s^{-1}]
57	ρ	density	[kg m^{-3}]
58	ϕ	area fraction, $\phi = A_f\,/\,A_c$	[-]
59			
60	*Subscripts*		
61	c	cavity	
62	f	fin	
63	i	initial	
64	L	phase change	
65	l	liquid	
66	m	melting	
67	*opt*	optimal	
68	*ref*	reference	

2

69	*s*	solid
70	*se*	sensible
71	*w*	wall

72 1. INTRODUCTION

73   The increase in energy demand, air pollution, energy prices, partial unavailability of fossil
74 fuels and environmental concerns are driving causes of studies on alternative methods of energy
75 production (Reddy, Mudgal, and Mallick 2018). As an extension, the development and application of
76 energy storage techniques has become a crucial part of this area. Among the different forms of energy
77 storage, thermal storage through sensible, latent or thermochemical heat (Zhang et al. 2016) has
78 become one of the most used in several applications (Hasnain 1998; Dabiri, Mehrpooya and Nezhad
79 2018; Zhu, Ma, and Wang 2009). The latent heat technique has become more attractive due to its
80 high energy storage capacity and the ability to provide heat at a constant temperature equal to the
81 material transition temperature. The materials used in latent heat energy storage are called Phase
82 Change Materials (PCM) (Ibrahim et al. 2017). These are classified according to their chemical
83 composition into organic (paraffin and non-paraffin), inorganic (salt and metal hydrates), and eutectic
84 (metal alloys) (Jamil et al., 2019, Ibrahim et al., 2017). As for the phase change temperature
85 classification, three groups are universally accepted: low, medium, and high temperature, Ehms et
86 al., 2019. According to Pielichowska et al., (2014), PCM is considered low temperature when the
87 phase change occurs at up to 15 °C, medium temperature when the phase change should occur
88 between 15 °C and 90 °C, and high temperature when the phase change occurs above 90 °C.

89   The selection of a PCM depends on its thermal properties, applications, stability and cost
90 (Aslfattahi et al., 2020). Their application can occur in many areas such as biomedicine, textile,
91 automotive (Jaguemont et al., 2018) and construction (Pielichowska and Pielichowski 2014,
92 Souayfane et al. 2016), solar power plants (Zhang et al. 2016, Khan et al. 2017) and electronic
93 components (Baby e Balaji 2012, Kalbasi and Salimpour, 2015). In buildings, PCM can be used for
94 cooling in passive or active systems (Souayfane et al. 2016). For example, one way of using PCM in
95 buildings is through the inclusion of micro-encapsuleted PCM in the materials used in construction
96 (Kalnaes et al., 2015). Another interesting application of PCM is in the temperature control of electric
97 car batteries. In this case, according to Jaguemont et al. (2018), PCM should have a melting point
98 between 45 °C and 50 °C to obtain greater efficiency. Solar absorption refrigeration systems can also
99 use PCM adapted to the working temperature, mass rate and loading and unloading time (Khan et al.
100 2017). Another interesting application refers to the use of PCM as thermal protection for food

101 products sensitive to thermal variations (Leducq et al. 2015). In terms of cooling electronic

102 components, Baby e Balaji (2012) studied experimentally the application of PCM with different types

103 of fins and at different power levels. It was found that, by including PCM in the finned cavity, the

104 electronic device showed a significant improvement in operating time.

105   PCMs have several advantages: small volumetric variation during phase change processes,

106 high specific heat and latent melting heat (Baby and Balaji 2012) as well as thermal stability

107 (Jaguemont et al. 2018). On the other hand, these materials have characteristic low thermal

108 conductivities which result in low charge and discharge rates (Akeiber et al. 2016; Pizzolato et al.

109 2017). Therefore, it is necessary to incorporate additional techniques to improve heat transfer between

110 the cavity and PCM. Among these techniques there are: multiple PCM usage (Ibrahim et al. 2017),

111 high thermal conductivity particle dispersion in the PCM (Wu et al. 2020), microencapsulation (Sun

112 et al. 2019) and fins. According to Kean et al. (2018), the inclusion of nanoparticles can reduce the

113 time of the melting or solidification processes. But, if nanoparticle concentration is in excess, a

114 negative effect may occur due to the agglomeration of material. In terms of thermal and enthalpic

115 stability with nanoparticle PCM, Aslfattahi et al. (2019) found an increase in thermal stability as well

116 as a decrease in melting point, compared to pure material.

117   Baby and Balaji (2012) studied experimentally the application of PCM to cool electronic

118 components. Different types of fins were investigated at different power levels. It was found that, by

119 including PCM in the finned cavity, the electronic device showed a significant improvement in

120 operating time. In general, fins result in an increase in active area and promote natural convection and

121 associated thermal processes such as phase change. Consequently, the natural convection process is

122 a defining parameter in the efficiency of finned systems. Fin geometry and positioning are also

123 important to the phase change process (Kazemi et al. 2018; Pu et al. 2020; Abdulateef et al. 2017). In

124 tubular systems, longitudinal fins placed at the bottom of the cavity allowed the formation of

125 recirculation zones which decreased PCM melting time (Kazemi et al. 2018). In comparison, tubular

126 systems with radial fins were also studied with variations in height and number of fins while keeping

127 the volume fraction and thickness constant (Pu et al. 2020). In this case it was determined that

128 configurations with longer fins decreased natural convection, reduced fin interactions and increased

129 melting time but an intermediate length was deemed the most adequate. Triple tube cavities were

130 studied with different configurations of rectangular and triangular fins (Abdulateef et al. 2017).

131 Results showed that placement of the fins affected substantially natural convection and could reduce

132 total melting times.

133   Several different fin geometric characteristics can be varied to evaluate their effect in PCM

134 melting. In the case of varying fin thickness in rectangular cavities, an optimum ratio of fin thickness

135 to combined fin + PCM volume which increased heat transfer rate through the fin but did not reduce

136 considerably heat transferred from the wall to the PCM was determined (Mostafavi, Parhizi, and Jain

137 2019). Fin thickness was also found to be directly proportional to heat transfer through it and inversely

138 proportional to temperature at its base, which improved cooling in the system (Arshad et al. 2020).

139 Fins of different geometries were also examined in the melting process of paraffin PCM with or

140 without nanoparticles (Kok 2020). In this case, fin geometries that probed into regions of un-melted

141 PCM resulted in more satisfactory results than conventional fins despite having less heat transfer

142 surface area. Melting lauric acid PCM was studied in rectangular cavities with 3 fins of different

143 widths and placement (Joshi and Rathod 2019). It was determined that reducing the width of upper

144 fins did not affect melting time but increased thermal storage capacity. Melting RT42 PCM was

145 studied numerically in rectangular cavities with two fins with varying lengths placed at different

146 heights while maintaining a constant total length (Ji et. al., 2018). It was proven that placement of

147 shorter fins higher and longer fins lower reduced total melting time when compared to two fins of

148 equal length. However, there was a limit to the length of the shorter fin, below which there were no

149 changes to melting time. Of these, fins are the most attractive due to ease of construction and low

150 manufacturing cost (Agyenim et al. 2010).

151   There are several studies in the literature on PCM melting/solidification in finned cavities.

152 However, studies of this type that maintain constant total fin area and PCM mass have not been found

153 in the literature. Thus, the objective of this study is to analyze the PCM melting process in a finned

154 rectangular cavity keeping both the PCM mass and the total fin area constant, thus changing only the

155 fin aspect ratio. With this, it becomes possible to determine the optimal aspect ratio to minimize the

156 total melting time for different fractions of the area between fin and cavity.

157

158 **2.1 Physical Domain**

159   The studied physical domain, depicted in Fig. 1, consisted of a two-dimensional rectangular

160 cavity with a width (W) of 50 mm and height (H) of 120 mm filled with lauric acid PCM initially in

161 a solid-state. A "negative fin", i.e. a morphing lateral intrusion, was positioned horizontally at the

162 center of the right wall with specified width (W_f) and height (H_f). A 2 mm opening was located in the

163 upper wall near the right side to simulate the loss of PCM from the cavity during the melting process.

164 While classical fin problems with a fixed temperature at its base do result in variations of temperature

along the length of the fin, the physical scale of the problem results in essentially a constant-temperature fin. This was observed in the experimental study of Kamkari and Shokouhmand 2014; and used to validate the numerical results of Joshi and Rathod 2019. So, it also was incorporated as a boundary condition in this work. The upper, lower, left side, front and rear walls were considered thermally insulated. This condition guaranteed null heat flow through these walls. Furthermore, with this condition, there was no temperature difference between the front and rear walls. Consequently, no considerable flow or circulation was expected to develop along this direction and the physical problem can be considered two-dimensional.
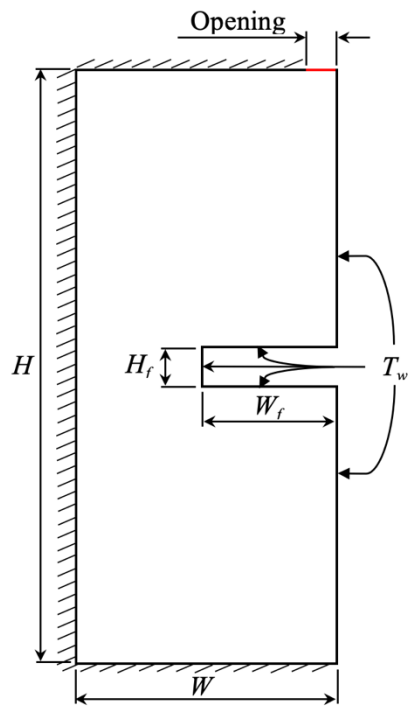
Figure 1 – 2D cavity domain with a morphing lateral intrusion shaped as a fin.

The constraints of the parametric study were the cavity area ($A_c = HW$) and the fin area ($A_f = H_f W_f$). Area A_c was kept constant and equal to 6,000 mm^2 while A_f was obtained from the area fraction $\left(\emptyset = A_f / A_c\right)$. Nine values of ϕ (0.005, 0.01, 0.02, 0.03, 0.04, 0.05, 0.1, 0.2 and 0.3) as well as nine values of W_f (10 mm, 15 mm, 20 mm, 25 mm, 30 mm, 35 mm, 40 mm, 45 mm and 48 mm) were selected. Through combinations of A_c, ϕ, and W_f, values of A_f and H_f were obtained and it was possible to calculate the fin aspect ratio $\left(RA_f = H_f / W_f\right)$. The selected values of ϕ and W_f resulted, ideally, in 81 geometric configurations. Of these, 3 of them could not be simulated as they exceeded the cavity dimensions and were discarded. Table 1 shows the dimensions of the remaining 78 fins.

Table 1 – Range of dimensions of fins tested.

		W_f [mm]								
		10	15	20	25	30	35	40	45	48
$\phi = 0.005$		3.00	2.00	1.50	1.20	1.00	0.86	0.75	0.67	0.63
$\phi = 0.01$		6.00	4.00	3.00	2.40	2.00	1.71	1.50	1.33	1.25
$\phi = 0.02$		12.00	8.00	6.00	4.80	4.00	3.43	3.00	2.66	2.50
$\phi = 0.03$		18.00	12.00	9.00	7.20	6.00	5.14	4.50	4.00	3.75
$\phi = 0.04$	H_f [mm]	24.00	16.00	12.00	9.60	8.00	6.86	6.00	5.33	5.00
$\phi = 0.05$		30.00	20.00	15.00	12.00	10.00	8.57	7.50	6.66	6.25
$\phi = 0.10$		60.00	40.00	30.00	24.00	20.00	17.14	15.00	13.33	12.50
$\phi = 0.20$			80.00	60.00	48.00	40.00	34.29	30.00	26.66	25.00
$\phi = 0.30$				90.00	72.00	60.00	51.43	45.00	40.00	37.50

The properties of lauric acid are shown in Tab. 2, Tab. 3 and Tab. 4. Table 2 presents the values of specific heat (c_p), density (ρ), temperature (T), and latent heat (L).

Table 2 - Properties of lauric acid (Adapted of Kamkari and Shokouhmand 2014).

Specific heat capacity solid/liquid [J/(kg K)]	2,180/2,390
Density solid/liquid [kg/m^3]	940/885
Melting temperature range [K]	316.65/321.35
Latent heat [J/kg]	187,210

Thermal conductivity (k) and dynamic viscosity (μ) of lauric acid as a function of temperature were obtained by linear interpolation and are presented in Tab. 3 and 4, respectively. It is worth mentioning that regarding the nonmetallic PCMs, heat conduction mainly relies on the vibration of the crystal lattice, as addressed by Wu et al. (2020). The lattice component of thermal conductivity strongly depends on the way the molecules are arranged. More specifically, the temperature increase leads to a weakening of the atomic bonds, which in turn causes heat transfer inhibition. Thus, the mechanism mentioned above justifies the feeble reduction of thermal conductivity with the augmentation of temperature illustrated in Tab. 3.

Table 3 - Thermal conductivity of lauric acid (Shokouhmand and Kamkari 2013).

T [K]	293	303	313	323	328	333	338	343
k [W/(m K)]	0.161	0.159	0.158	0.145	0.143	0.142	0.139	0.138

Table 4 - Dynamic viscosity of lauric acid (Valeri and Meirelles 1997).

T [K]	321.2	322	333	344	355	372	383
μ [kg/(m s)]	0.00760	0.00747	0.00542	0.00428	0.00338	0.00250	0.00210

2.2 Mathematical Model

The mathematical model used to represent the melting process consisted of the equations of conservation of mass, momentum and energy shown in Eq. (1-3), respectively:

$$\frac{\partial \rho}{\partial t} + \nabla\left(\rho \vec{V}\right) = 0 \tag{1}$$

$$\frac{\partial}{\partial t}\left(\rho \vec{V}\right) + \nabla\left(\rho \vec{V}\vec{V}\right) = \nabla\left(\mu \nabla \vec{V}\right) - \nabla p + \rho \vec{g} + \vec{S} \tag{2}$$

$$\frac{\partial}{\partial t}\left(\rho \lambda\right) + \nabla\left(\rho \vec{V}\lambda\right) = \nabla\left(k \nabla T\right) \tag{3}$$

where $\vec{V}$ represents the velocity vector, t is the time, p is the pressure, $\vec{g}$ is the acceleration of gravity, $\vec{S}$ is the source term, and λ is the total enthalpy. The total enthalpy is obtained by adding the change in enthalpy associated with phase change (λ_L) and sensible enthalpy (λ_{se}), obtained through Eq. (4):

$$\lambda_{se} = \lambda_{ref} + \int_{T_{ref}}^{T} c_p \, dT \tag{4}$$

where λ_{ref} is the enthalpy at the reference temperature ($T_{ref} = 298$ K). The enthalpy in phase change is calculated as $\lambda_L = \beta L$.

For the PCM melting process, an enthalpy porosity model (Voller and Prakash 1987) was used. The model treated the solid-liquid interface zone (mushy zone) as a porous zone with the source term obtained from Eq. (5):

$$\vec{S} = \frac{(1-\beta)^2}{(\beta^3 + \varepsilon)} C\vec{V} \tag{5}$$

where β is the liquid fraction, ε is a constant with value of 0.001 used to prevent division by zero and C is the porous zone constant. This constant depends on the morphology of the porous zone (Voller

222 and Prakash 1987). The net fraction of PCM within the phase change range is calculated from Eq.

223 (6):

$$\beta = \begin{cases} 0 & se & T < T_S \\ 1 & se & T > T_l \\ T - T_S / T_l - T_S & se & T_S < T < T_l \end{cases} \tag{6}$$

225   The boundary conditions adopted were of adiabatic left, lower and upper walls of the domain,

226 shown in Eq. (7-9), respectively:

$$-k\frac{\partial T}{\partial x}\Big|_{\substack{x=0 \\ y=0-H}} = 0 \tag{7}$$

$$-k\frac{\partial T}{\partial y}\Big|_{\substack{x=0-W \\ y=0}} = 0 \tag{8}$$

$$-k\frac{\partial T}{\partial y}\Big|_{\substack{x=W-opening \\ y=0}} = 0 \tag{9}$$

230 while a prescribed temperature condition was applied on the right vertical wall, all fin surfaces and

231 the opening, as shown in Eq. (10, 11), respectively:

$$T\Big|_{\substack{x=W \\ y=0-H}} = T_w \tag{10}$$

$$T\Big|_{\substack{x=opening \\ y=H}} = T_a \tag{11}$$

234 **3 Numerical Model**

235   Numerical simulations were performed on ANSYS FLUENT® and the computational meshes

236 were created on ANSYS ICEM® version 18.2. In the reference experimental work of Kamkari and

237 Shokouhmand (2014), the liquid PCM was removed manually. In the present numerical work, this

238 PCM removal was modeled through the "*pressure-outlet*" boundary condition imposed on the

239 opening, with gauge pressure of 0 Pa and temperature of 343 K. For the pressure correction and

240 pressure-velocity coupling, the "*presto*" and "*simple*" criteria were adopted, respectively. The flow

241 was considered laminar transient with a time step of 0.1 s. In the energy and momentum equations, a

242 "*first-order upwind*" scheme was used. Absolute convergence criteria of 10^{-8} for the energy equation

243 and 10^{-5} for the velocity and continuity equations were adopted. Relaxation coefficients used were:

9

244 0.15 for pressure and momentum, 0.3 for density, field forces and energy and 0.2 for the liquid

245 fraction. Intermediate values of k e μ were obtained by linear interpolation of the data of Tab. 3 and

246 Tab. 4. The value of ρ_s was considered constant as of Tab. 2; however, values of ρ_l were pre-set from

247 reference (Chuah et al. 2006) according to temperature: 885 kg/m^3 at 321.35 K (Tab. 1), 870 kg/m^3

248 at 323 K and 862 kg/m^3 at 333 K. The lower, upper, and left walls of the cavity were defined as

249 adiabatic. The right wall and the fin surfaces were kept at the heating temperature $T_w = 343$ K. The

250 no-slip condition was applied in all walls and the fin surfaces, except for the opening, which was

251 considered free flow at $T_a = 343$K. In addition, the PCM was subjected to an initial temperature of T_i

252 =298 K.

253

254 **3.1 Model Validation and Mesh Test Sensitivity**

255 *3.1.1 Model Validation*

256 Numerical validation was performed with comparisons to reference experimental data

257 (Kamkari and Shokouhmand 2014) in two ways: through liquid fraction field and with the liquid

258 fraction profile over time. The reference study consisted of the melting process of lauric acid PCM in

259 a similar physical domain. The experimental rectangular cavity measured 50 mm in width, 120 mm

260 in height and 120 mm in thickness, with a fin 25 mm in width and 4 mm in height. The fin and the

261 right wall were subjected to a constant temperature of 343 K while the remaining walls were thermally

262 insulated. The PCM was initially at a temperature of 298 K, i.e., solid-state (Kamkari and

263 Shokouhmand 2014).

264 Figure 2 shows a comparison of liquid fraction fields (β) from the reference experimental

265 study (Kamkari and Shokouhmand 2014) and the present numerical study at 10 min, 30 min and 50

266 min of the melting process. Figures 2(a, c, e) contain the experimental results and Figs. 2(b, d, f) the

267 numerical results. In the numerical results, white and blue colors represent the solid-state PCM, while

268 black and red colors represent the liquid state. As seen in Fig. 2, there is good visual agreement in the

269 liquid fraction between both sets of results for all melting times.

270
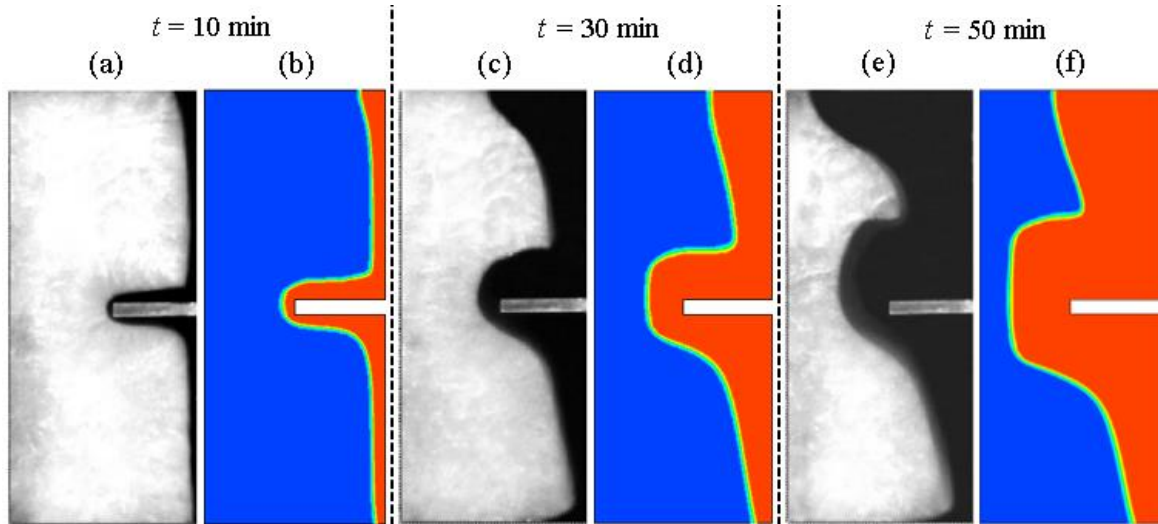
271 Figure 2 - *β* distribution at time t = 10 min, 30 min and 50 min: (a), (c) and (e) experimental results (Kamkari

272 and Shokouhmand 2014); (b), (d) and (f) present numerical results.

273   Furthermore, Fig. 3 shows transient profiles of *β* obtained experimentally (Kamkari and

274 Shokouhmand 2014) and numerically (present study). The values of *β* range from 0 to 1, with 0

275 representing the solid-state PCM and 1 representing the liquid state. Coherent agreement can be

276 clearly observed between the numerical and experimental results. The average difference was

277 approximately 5.4%, while the maximum difference was approximately 6.3% at t = 110 min with

278 *β* = 0.856.

279
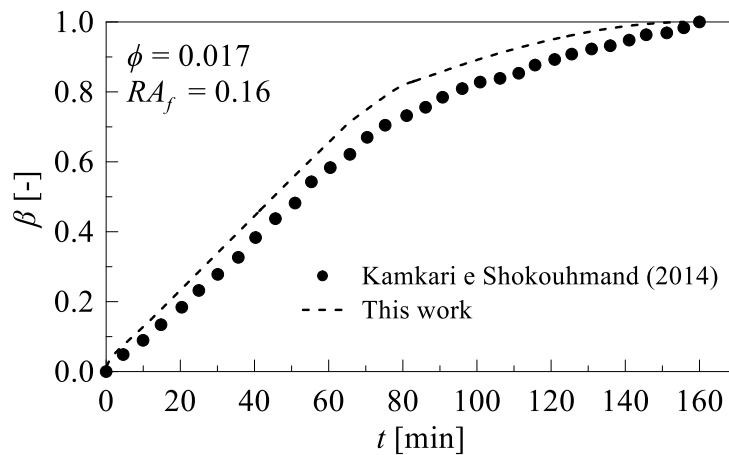
280   Figure 3 – Liquid fraction *β* as function of time t: comparison between experimental results (Kamkari and

281 Shokouhmand 2014) and present numerical results.

282

283   Considering the good agreement between the numerical results of the present study and

284 reference experimental results (Kamkari and Shokouhmand 2014), both qualitative (Fig. (2)) and

quantitative (Fig. (3)), as well as the constant value assigned to C (seen in Section 3.1.3), the numerical model used in this study was considered validated.

3.1.2 Mesh Test Sensitivity

For the present numerical study, three computational meshes were created, as seen in Fig. 4, with increasing number of elements. Meshes (a), (b) and (c) contained 10,118, 14,520 and 28,457 elements, respectively. Mesh independence analysis was performed using the GCI (Grid Convergence Method) procedure (Celik et al. 2008) by comparing the most refined mesh (c) with the intermediate mesh (b) and the least refined mesh (a). The calculated percentage rates were 1.9% and 5.5%, respectively. Thus, with a GCI of 1.9%, mesh (c) with 28,457 elements mesh was considered suitable for numerical simulations.
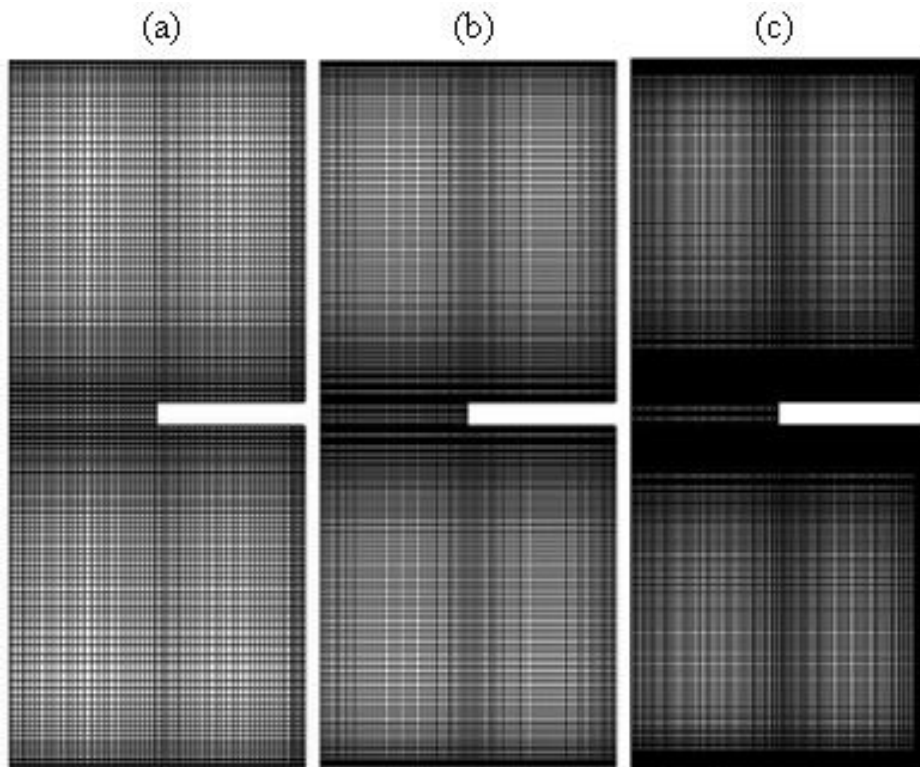
Figure 4 – Grid convergence study meshes: (a) 10,118, (b) 14,520 and (c) 28,457 elements.

3.1.3 Adjustment of porous zone constant "C"

The porous zone constant (C) of Eq. (5) indicated the material velocity damping to zero in the solid phase and its value had to be adjusted according to the problem analyzed. By definition, the value of C should be sufficient to allow flow in the transition region while at the same time

303 suppressing velocity in the solid phase (Voller and Prakash 1987). For the present study, a range of
304 several orders of magnitude of C values were tested. It was observed that a value of C = 10^{11} more
305 satisfactorily reproduced the PCM merging process and, consequently, was kept for all the numerical
306 results presented in this study.

307

4. RESULTS AND DISCUSSIONS

309 The objective of this study was to analyze the influence of fin aspect ratio $\left(RA_f = H_f/W_f\right)$,
310 and obtain the optimal aspect ratio (RA_{opt}), thereby minimizing the melting process time for each ϕ.
311 For clarity, each parameter affecting optimization was analyzed individually.

312

4.1 Effects of Buoyancy on the Melting Process

314 Figures 5(a, b) show the velocity fields for $RA_f = 0.288$ and $\phi = 0.03$ at times t = 20 min and
315 40 min, respectively. In the figures, PCM is represented with gray color in the solid phase and black
316 color in the liquid phase, with the velocity field at the same instant of time superimposed. It can be
317 seen in both figures that, due to the buoyancy force generated by the variation of temperature within
318 the liquid phase, an upward flow is present close to the heated wall (right) and in the region above
319 the fin. Downward flow can also be observed at the solid-liquid interface, thus ensuring the principle
320 of mass conservation. In between these two convective currents and their velocity profile, it is
321 possible to observe a shear region captured by the proper refinement of the computational mesh
322 throughout the domain. Heating occurs along the upper side of the fin and beyond the reach of the
323 vertical wall. In this region, a large recirculation zone is observed and can be classified as Rayleigh-
324 Bénard convection. A similar flow can also be observed between the base of the cavity and the base
325 of the fin, producing another recirculation zone in this region but with different characteristics.
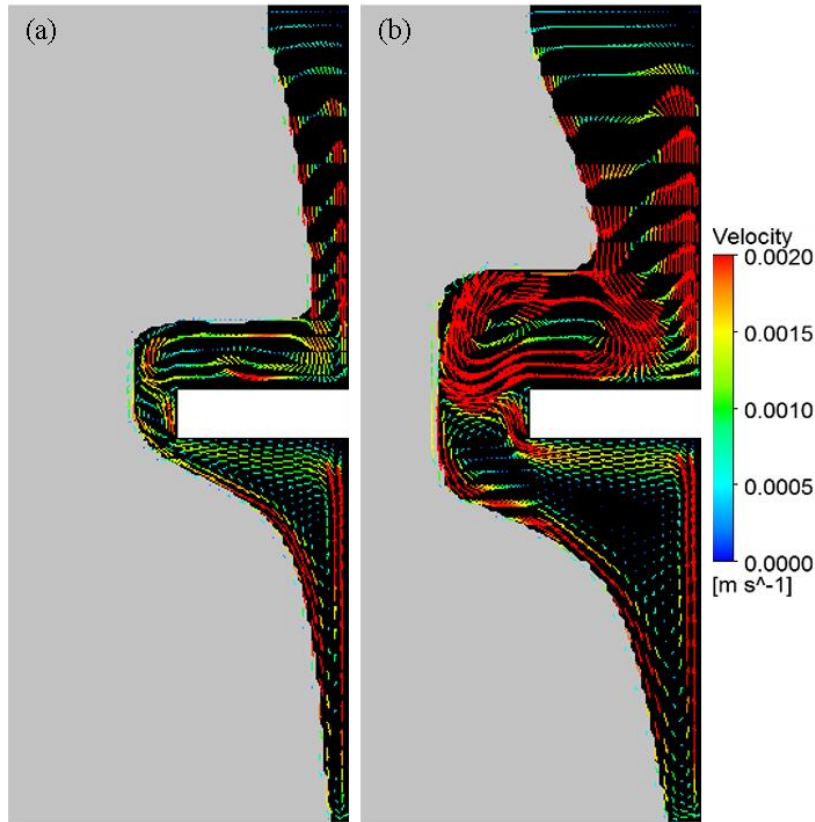
326

Figure 5 – Velocity distribution for $RA_f = 0.288$ and $\phi = 0.03$ at: (a) t = 20 min, (b) t = 40 min.
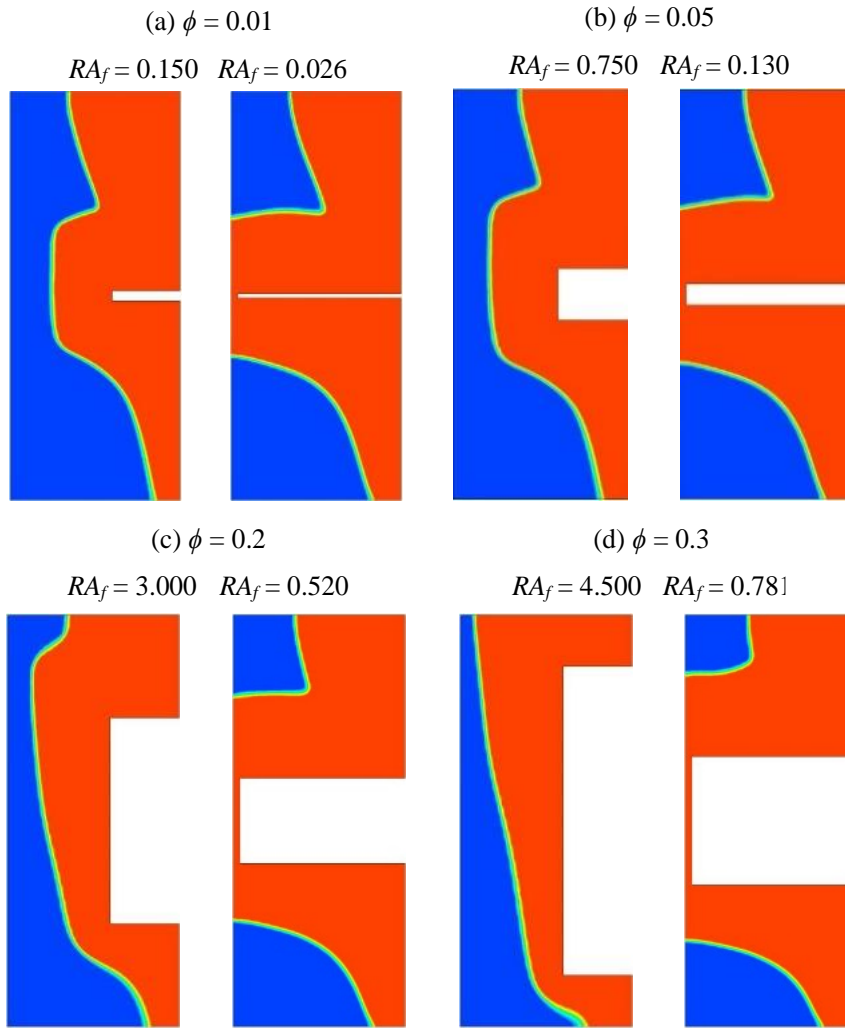
Figures 6(a, b) show temperature fields for $RA_f = 0.450$ and 0.078 with $\phi = 0.03$ at times t = 10 min and 50 min, respectively. In the figures, for all presented results, a robust thermal gradient near the right vertical wall and the entire perimeter of the fin can be initially observed. Strong thermal stratification is detected in the cavity at the final t = 50 min moment and especially in the region above and below the fin. Buoyant forces arising from the change in density near the active vertical wall form an upward convective current seen in Fig. 5(b). This current stratifies thermally the liquid PCM in the upper part of the cavity. A similar condition is observed below the fin for both tested values of RA_f, which contributes to the formation of a curved melting front. However, at t = 10 min and t = 50 min, there is an increase in thermal stratification in the region below the fin with decreasing RA_f. This behavior is related to the increase in fin perimeter, which limits the movement of the upward convective currents to the top of the cavity and contributes to accelerate the melting process. Slight temperature variations at the top of the fin at t = 10 min for both tested values of RA_f have also been detected. These characteristics fused layer instabilities are associated with Rayleigh-Bénard convection formation. Finally, it is worth mentioning that, for the others tested values of area fraction ϕ, this behavior is also observed.

14
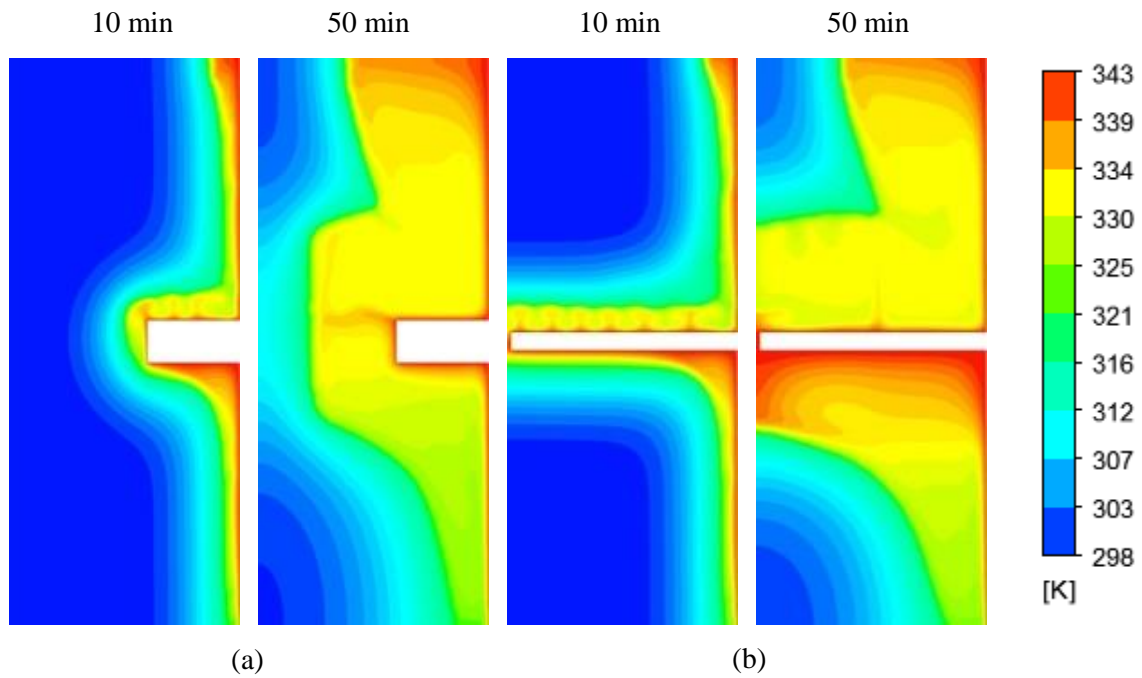
Figure 6 – Temperature distribution at t = 10 and 50 min, $\phi = 0.03$ and: (a) $RA_f = 0.450$ and (b) $RA_f = 0.078$.

4.2 Area Fraction Effect

Figures 7(a-d) show the liquid fraction (β) fields at time t = 50 min for $W_f = 20$ mm and 48 mm and area fractions of $\phi = 0.01$, 0.05, 0.2 and 0.3, respectively. In the figures, the first and third columns present β fields with respect to the case $W_f = 20$ mm; similarly, the second and fourth columns are with respect to $W_f = 48$ mm. As observed in Fig. 7(a-d), there is a reduction of the total time of the melting process for any ϕ with an increase in the fin width W_f, which also corresponds to a reduction in the value of RA_f. In addition, it can be seen that the liquid fraction fields near the right vertical wall are similar to each other for both $W_f = 20$ mm and $W_f = 48$ mm, featuring a thin layer of molten PCM for different RA_f and ϕ values. It is also noted that at t = 50 min and for $\phi = 0.01$ to 0.05, within different values of RA_f, the solid-liquid interface profiles are similar to each other, differing only in the region to the left of the fin between $W_f = 20$ mm and $W_f = 48$ mm.

15

358

(a) $\phi = 0.01$

$RA_f = 0.150$ $RA_f = 0.026$

(b) $\phi = 0.05$

$RA_f = 0.750$ $RA_f = 0.130$

(c) $\phi = 0.2$

$RA_f = 3.000$ $RA_f = 0.520$

(d) $\phi = 0.3$

$RA_f = 4.500$ $RA_f = 0.781$

359

360   Figure 7 – β field at t = 50 min, W_f = 20 and 48 mm: (a) ϕ = 0.01; (b) ϕ = 0.05; (c) ϕ = 0.2 and (d) ϕ = 0.3.

361

4.3 Effect of Fin Aspect Ratio (RA_f)

The different heat transfer mechanisms in a melting process can be identified by varying the Nusselt number ($Nu = h\,L_c/k_l$) as a function of Fourier number ($Fo = \alpha_l\,t/L_c^2$), where L_c is the characteristic length $\left(L_c = A_c^{1/2}\right)$, A_c is the cavity area, h is the heat transfer coefficient $\left(h = q''/(T_w - T_l)\right)$, q'' is the heat flux on the right sidewall and fin perimeter, T_w (343 K) is the wall temperature, T_l is the PCM liquid temperature and α_l $\left(\alpha_l = k_l/\rho_l\,c_{p\,l}\right)$ is the liquid thermal diffusivity. The heat flux (q'') was obtained on CFX-Post from the results obtained from Fluent.

16

369   Figure 8(a-f) shows Nu profiles as a function of Fo for different RA_f and $\phi = 0.01, 0.03, 0.05$,

370   0.1, 0.2, and 0.3, respectively. As seen in the figure, regardless of the values of RA_f and ϕ, all results

371   show 3 different regions: I – with a marked reduction of Nu in the initial moments; II - with Nu values

372   without large variations, despite fluctuations in most of the melting process and III – a sharp reduction

373   of Nu in the final moments. More specifically, the low thermal resistance of the thin wall-melted

374   PCM layer in the initial moments allows the characterization of region I as conductive. With the

375   beginning of the melting process, still in region I, there is an increase in the size of the liquid layer.

376   This behavior induces a change in the heat transfer mechanism from conductive to convective

377   represented by region II. In region II, Nu continues to decrease but more slowly. This behavior is in

378   accordance with reference work (Ji et al. 2018) and corroborates with the observations on the velocity

379   fields (Fig. 5): heating at the fin tip produces recirculation of the Rayleigh-Bénard liquid PCM which

380   generates, in turn, fluctuations in the local temperature. Consequently, Nu also has fluctuations as

381   seen in region II of Fig. 8(a-f). These oscillations decrease as the solid-liquid interface moves away

382   from the fin in accordance with known experimental behavior (Kamkari and Shokouhmand 2014).

383   In addition, regarding Fig. 8(a-f), it can be observed that smaller values of RA_f ($RA_f = H_f / W_f$) are

384   associated with longer periods of Nu fluctuations. This behavior is due to the increase of W_f.

385   Moreover, it is observed that increasing the value of ϕ reduces the amplitude of the instabilities, which

386   is visually evident in a comparison of Fig. 8(a) and 8(f). This fact justifies the reduction of the time

387   difference of the melting process with increasing of ϕ seen in the analysis of the liquid fraction

388   profiles. In region III, at the final moments, Nu number again decreases more sharply due to the

389   reduction of the heat transfer rate resulting from weakening convection currents. In this figure it can

390   also be observed that, for all values ϕ and near $Fo = 0.05$, there is a small increase in Nu for the

391   highest RA_f values. This behavior occurs due to the greater length of the solid-liquid PCM interface,

392   as seen in Fig. 7(a-d). For example, in Fig. 7(a) for ϕ=0.01, the length of the solid-liquid interface for

393    $RA_f = 0.15$ is greater than for $RA_f = 0.026$, resulting in a larger Nu seen in Fig. 8(a). As a final point,

394   it should be mentioned that for all tested ϕ values, the cases with the lowest Nu are those that presented

395   the fastest melting processes.

396
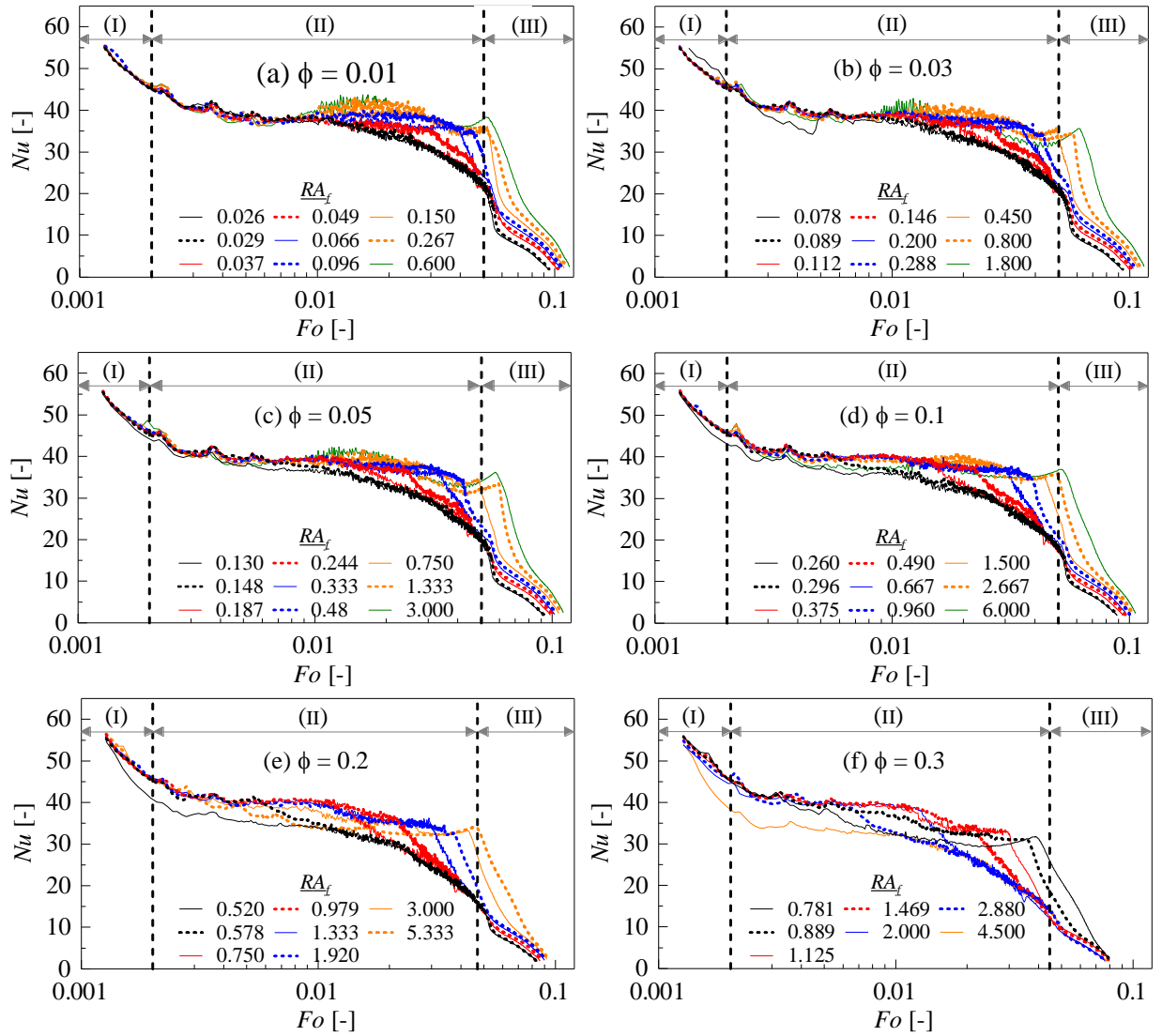
Figure 8 – Nu vs. Fo, for several values of RA_f and: (a) $\phi = 0.01$; (b) $\phi = 0.03$; (c) $\phi = 0.05$; (d) $\phi = 0.1$; (e) $\phi = 0.2$ and (f) $\phi = 0.3$.

Figures 9(a-c) show β fields for $\phi = 0.005$ at times t = 1 min, 10 min, 30 min, 50 min, 70 min and 90 min and $RA_f = 0.300$, 0.033 and 0.013, respectively. As in Fig. 7, blue color represents the solid phase and red color represents the liquid phase. Initially, it is observed that at t = 1 min, regardless of the values of RA_f, the fused PCM layer in the vicinity of the heated wall is very thin. At this time, the PCM is almost entirely in the solid phase and the heat transfer process is predominantly conductive. As t increases, the thickness of the molten layer increases and buoyant forces become predominant in relation to viscous ones; therefore, a change in the heat transfer mechanism occurs, becoming convective. As a result, solid-phase erosion occurs in the upper cavity at the solid-liquid interface, forming a curvature of the melting front. This can be observed in Fig 9 for all values of RA_f

410   at t = 30 min, 50 min and 70 min. Additionally, it is noted that RA_f also influences the melting rate.

411   For example, after the initial moments, there is a tendency to accelerate the PCM merger process with

412   reduced RA_f. This is mainly identified at t = 50 min, where it can be observed that the melting rate for

413   RA_f = 0.013 is much larger than for RA_f = 0.3. This behavior is due to the augmented perimeter of the

414   fin inserted in the PCM, which increases the heat transfer area between the fin and the PCM.

415
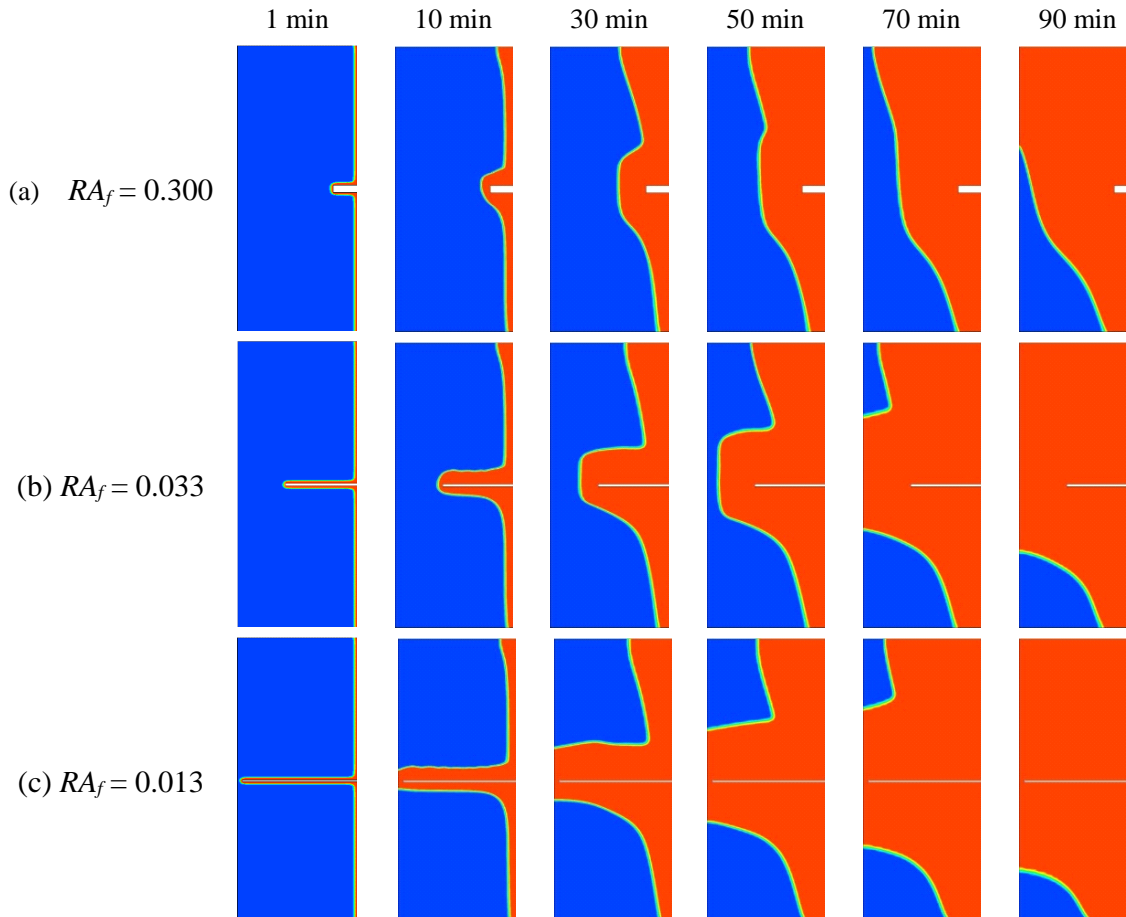
416   Figure 9 – β field for ϕ = 0.005, t = 1 min, 10 min, 30 min, 50 min, 70 min and 90 min, and: (a) RA_f = 0.300;

417   (b) RA_f = 0.033 and (c) RA_f = 0.013.

418

419   In quantitative terms, the influence of RA_f (H_f /W_f) over β is shown in Fig. 10(a-f) which

420   highlights the variations of β as a function of time for different RA_f and ϕ = 0.01, 0.03, 0.05, 0.1, 0.2

421   and 0.3, respectively. Overall, higher values of RA_f are associated with longer complete PCM melting

422   times (β = 1) independent of the area fraction ϕ. Moreover, since the increase in RA_f leads to fins with

423   smaller heat exchange area, the heat removal (per unit time) process ends up being penalized.

424   Conversely, it can be demonstrated that there is a gradual tendency of acceleration of the melting

425   process with the gradual reduction of the aspect ratio RA_f for all tested values of ϕ, even if it is not

426   evident which were the smallest calculated RA_f values.
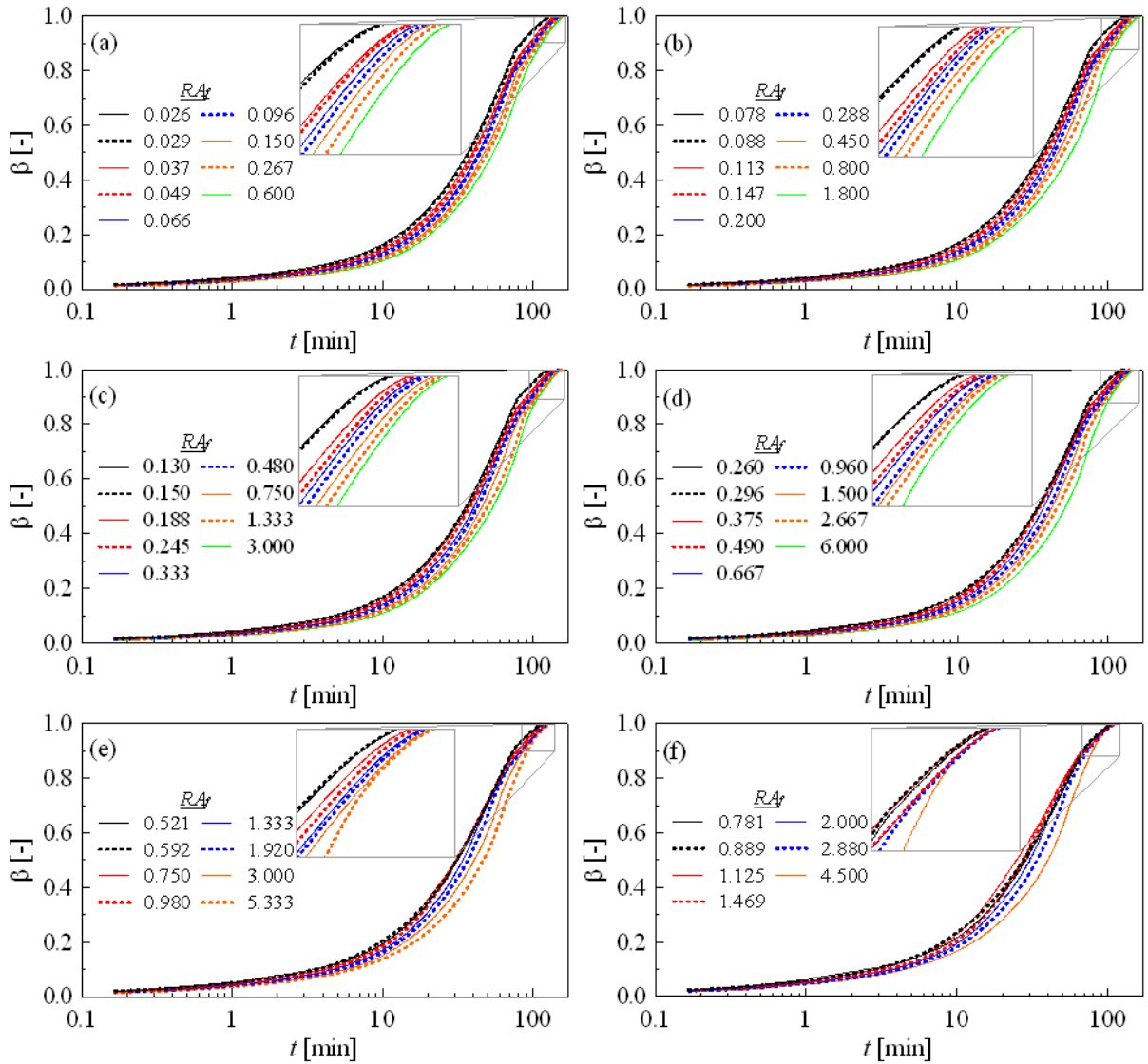
Figure 10 – β vs. t for several values of RA_f and: (a) $\phi = 0.01$; (b) $\phi = 0.03$; (c) $\phi = 0.05$; (d) $\phi = 0.1$; (e) $\phi = 0.2$ and (f) $\phi = 0.3$.

A deeper understanding of how the total melting time is affected by the various parameters can be obtained from Fig. 11: it shows the maximum time of the melting process ($\beta = 1$) as a function of RA_f for all the simulated values of ϕ of all 78 configurations. It can be immediately observed that increases of ϕ are associated with decreases in the time required for the PCM to completely melt. For example, at $RA_f = 1$ and for $\phi = 0.02$ and 0.2, the maximum melting times were approximately 165 min and 127 min, respectively. Therefore, the increase of an order of magnitude in the ϕ value led to a reduction of approximately 38 min in the melting process.

20
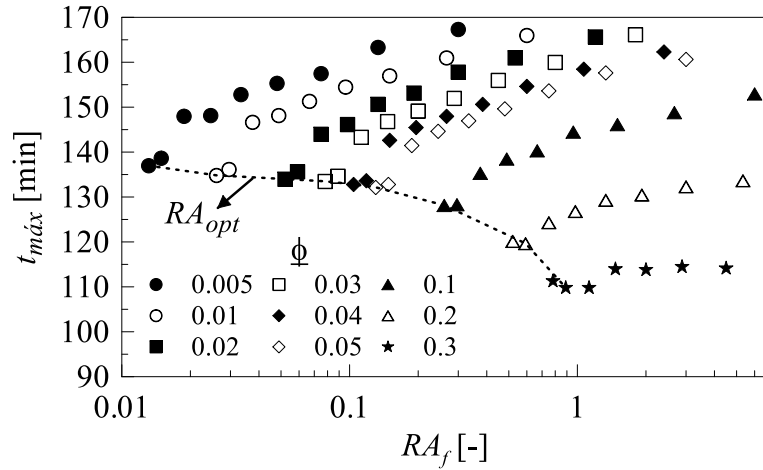
Figure 11 – Maximum melting time of each fin configuration as function of RA_f and several values of ϕ.

For this study the optimum aspect ratio (RA_{opt}) was defined as the one with the lowest melting rate, i.e. the shortest time to reach complete melting for each ϕ. For ϕ ranging from 0.005 to 0.1, the shortest melting times were obtained with the lowest RA_f. However, for $\phi = 0.2$ and 0.3, the shortest time occurred in the "second lowest" RA_f, which were designated the proper RA_{opt}. The total trend of the RA_{opt} values is plotted in Figure 12 as a dashed line. Similar behavior was observed for this configuration in other studies (Biserni, Rocha, and Bejan 2004) in which the optimal geometries proved to be the ones which permitted, as far as possible, the morphing "inverted fins" to penetrate the cavity. The optimal values of aspect ratios found in this study are shown in Table 5 with respect to tested values of ϕ.

Table 5 - RA_{opt} at corresponding values of ϕ.

ϕ	0.005	0.01	0.02	0.03	0.04	0.05	0.1	0.2	0.3
RA_{opt}	0.013	0.026	0.052	0.078	0.104	0.130	0.260	0.592	0.889

Further work was conducted with the investigation of the absorbed energy. Since the cavity area (A_c) was constant, the fin area (A_f) obviously increased with increases of the area fraction ($\phi = A_f/A_c$). Under these conditions, increasing ϕ implied a reduction in the amount of mass contained in the cavity and the resulting variation in the energy absorbed by it. This behavior can be observed in Fig. 12, which shows the total energy absorbed by the cavity as a function of time for the optimal aspect ratios RA_{opt} with respect to all tested area fractions ϕ. It can be noticed that, as ϕ increases, there is a reduction in absorbed energy as predicted. For example, between $\phi = 0.1$ and $\phi = 0.3$ at $t = 100$ min, the energy absorbed is approximately 861 kJ and 690 kJ, respectively. This represents a reduction of around 20% in terms of absorbed energy. However, for a variation of 10% in area fraction

462   ($\phi = 0.005$ and $\phi = 0.05$) at t = 100 min, the absorbed energy is around 935 kJ and 902 kJ, respectively.

463   These values represent a decrease of only approximately 3% of absorbed energy. Based on these

464   results, it can be concluded that the reduction of the absorbed energy should be significant only for

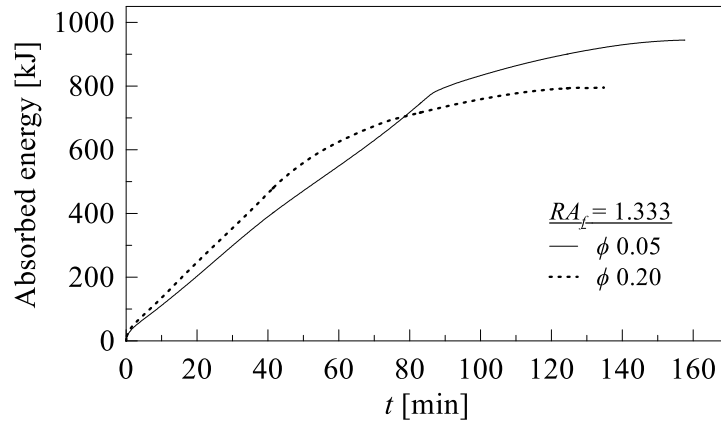465   values of ϕ greater than a threshold value of 0.05.
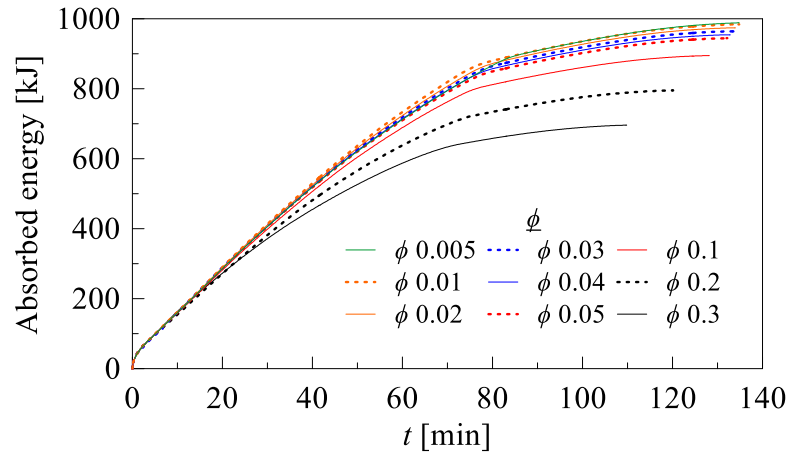
466

467   Figure 12 – Cavity absorbed energy over time with respect to the optimal aspect ratios, RA_{opt} and several ϕ

468   values.

469   Finally, Fig. 13 shows the variation of the energy absorbed in the cavity as a function of time

470   with respect to the cases $RA_f = 1.33$ and $\phi = 0.05$ and 0.2. Figure 13 shows a clear inversion in trend

471   at a time of approximately 80 min. For times shorter than 80 min, an increase in ϕ results in an increase

472   in absorbed energy. For example, at t = 60 min and $\phi = 0.05$ and $\phi = 0.2$, approximately 549 kJ and

473   625 kJ were absorbed, respectively. This represents an increase of 12% in absorbed energy when ϕ is

474   increased from 0.05 to 0.2. This behavior may be of great interest in applications that require a high

475   storage rate in shorter times. In contrast, for times longer than 80 min, the opposite behavior is

476   observed with a decrease in ϕ resulting in an increase in absorbed energy. For example, at t = 120

477   min, for $\phi = 0.05$ and 0.2, approximately 890 kJ and 790 kJ were absorbed, respectively. This

478   demonstrates that a 15% increase in area fraction resulted in approximately an 11% reduction in total

479   energy absorption.

480

481 Figure 13 – Absorbed energy over time for RA_f = 1.33 and ϕ = 0.05 and 0.2.

Plot of Absorbed energy [kJ] (y-axis, 0 to 1000) versus t [min] (x-axis, 0 to 160). Legend: RA_f = 1.333, — ϕ 0.05, ···· ϕ 0.20.

482

483 **5. Conclusions**

484   The present work was concerned with the effect of the aspect ratio of an "inverted fin", i.e. an
485 intrusion placed in a rectangular cavity, in the melting process of lauric acid PCM. Results were
486 obtained by means of a computational model based on the equations of conservation of mass,
487 momentum, energy and an enthalpy-porosity model representing the PCM melting process. The main
488 conclusions were:

489 • a shear region between two convective currents was observed. This was a result of a buoyant
490   upward flow in the region above the fin and a downward flow at the solid-liquid interface.
491   Another region with great recirculation was observed between the base of the cavity and the base
492   of the fin. In addition, the existing circulation along the top of the fin was classified as Rayleigh-
493   Bénard convection.

494 • for all tested values of area fraction (ϕ), there was a reduction in total time of the melting process
495   with a reduction of the value of the fin aspect ratio RA_f, caused by the increase of the fin width
496   W_f. It was also noted that at t = 50 min for ϕ ranging from 0.01 to 0.05, with different values of
497   RA_f, the solid-liquid interface profiles were similar to each other, differing only in the region to
498   the left of the fin between W_f = 20 mm and W_f = 48 mm.

499 • Nu profiles as a function of Fo for different RA_f and ϕ = 0.01, 0.03, 0.05, 0.1, 0.2 and 0.3 showed
500   3 distinct regions. Region I presented a marked reduction of Nu in the initial moments (mostly
501   due to conduction). Region II presented Nu values without large variations but with fluctuations
502   in most of the melting process (mostly due to convection). Region III presented sharp reductions
503   of Nu in the final moments, due to the weakening of convection currents.

504 • The various parameters affecting the total melting time were investigated with reference to the
505   78 simulated configurations. The increase of ϕ was associated with decreasing times required

23

for the PCM to completely melt. For example, for $RA_f = 1$ and $\phi = 0.02$ and 0.2, the maximum melting times were approximately 165 min and 127 min, respectively. Therefore, the increase of an order of magnitude in the value of ϕ led to a reduction of approximately 38 min in the melting process.

- Finally, an investigation regarding the amount of absorbed energy with respect to RA_{opt} was carried out. It was noticed that there was a reduction in absorbed energy as ϕ increased. For example, at t = 100 min for $\phi = 0.1$ and $\phi = 0.3$, the energy absorbed was approximately 861 kJ and 690 kJ, respectively. This represented a reduction of around 20% in terms of absorbed energy. However, for an increase of 10% of area fraction ($\phi = 0.005$ to $\phi = 0.05$) at t = 100 min, the absorbed energy was around 935 kJ and 902 kJ, respectively. These values represented a decrease of 3% of absorbed energy. With these results, it was concluded that the reduction of the absorbed energy was significant only for ϕ greater than a threshold value of 0.05.

References

Abdulateef, Ammar M., Sohif Mat, Kamaruzzaman Sopian, Jasim Abdulateef, and Ali A. Gitan. 2017. "Experimental and Computational Study of Melting Phase-Change Material in a Triplex Tube Heat Exchanger with Longitudinal/Triangular Fins." *Solar Energy* 155: 142–53. https://doi.org/10.1016/j.solener.2017.06.024.

Agyenim, Francis, Neil Hewitt, Philip Eames, and Mervyn Smyth. 2010. "A Review of Materials, Heat Transfer and Phase Change Problem Formulation for Latent Heat Thermal Energy Storage Systems (LHTESS)." *Renewable and Sustainable Energy Reviews* 14 (2): 615–28. https://doi.org/10.1016/j.rser.2009.10.015.

Akeiber, Hussein, Payam Nejat, Muhd Zaimi Abd Majid, Mazlan A. Wahid, Fatemeh Jomehzadeh, Iman Zeynali Famileh, John Kaiser Calautit, Ben Richard Hughes, and Sheikh Ahmad Zaki. 2016. "A Review on Phase Change Material (PCM) for Sustainable Passive Cooling in Building Envelopes." *Renewable and Sustainable Energy Reviews* 60: 1470–97. https://doi.org/10.1016/j.rser.2016.03.036.

Arshad, Adeel, Mark Jabbal, Pouyan Talebizadeh Sardari, Muhammad Anser Bashir, Hamza Faraji, and

538   Yuying Yan. 2020. "Transient Simulation of Finned Heat Sinks Embedded with PCM for Electronics

539   Cooling." *Thermal Science and Engineering Progress* 18 (August).

540   https://doi.org/10.1016/j.tsep.2020.100520.

541   Aslfattahi, Navid, R. Saidur, Mohd Faizul Mohd Sabri, and A. Arifutzzaman. 2019. "Experimental

542   Investigation of Thermal Stability and Enthalpy of Eutectic Alkali Metal Solar Dispersed with MGO

543   Nanoparticles." *International Journal of Technology* 10 (6): 1112-1119.

544   https://dx.doi.org/10.14716/ijtech.v10i6.3568.

545   Aslfattahi, Navid, R. Saidur, A. Arifutzzaman, R. Sadri, Nuno Bimbo, Mohd Faizul Mohd Sabri, Philip A

546   Maughan, Luc Bouscarrat, Richard J. Dawson, Suhana Mohd Said, Boon Tong Goh, and Nor Azwadi

547   Che Sidik. 2020. "Experimental investigation of energy storage properties and thermal conductivity of

548   a novel organic phase change material/MXene as A new class of nanocomposites." *Journal of Energy*

549   *Storage* 27: 101115. https://doi.org/10.1016/j.est.2019.101115.

550   Baby, Rajesh, and C. Balaji. 2012. "Experimental Investigations on Phase Change Material Based Finned

551   Heat Sinks for Electronic Equipment Cooling." *International Journal of Heat and Mass Transfer* 55

552   (5–6): 1642–49. https://doi.org/10.1016/j.ijheatmasstransfer.2011.11.020.

553   Biserni, C., L. A.O. Rocha, and A. Bejan. 2004. "Inverted Fins: Geometric Optimization of the Intrusion into

554   a Conducting Wall." *International Journal of Heat and Mass Transfer* 47 (12–13): 2577–86.

555   https://doi.org/10.1016/j.ijheatmasstransfer.2003.12.018.

556   Celik, Ismail B., Urmila Ghia, Patrick J. Roache, Christopher J. Freitas, Hugh Coleman, and Peter E. Raad.

557   2008. "Procedure for Estimation and Reporting of Uncertainty Due to Discretization in CFD

558   Applications." *Journal of Fluids Engineering, Transactions of the ASME* 130 (7): 0780011–14.

559   https://doi.org/10.1115/1.2960953.

560   Chuah, T.G., D. Rozanna, A. Salmiah, S. Y. Thomas Choong, and M. Sa'ari. 2006. "Fatty Acids Used as

561   Phase Change Materials (PCMs) for Thermal Energy Storage in Building Material Applications."

562   *Applied Energy*, no. July: 123–37.

563   Dabiri, Soroush, Mehdi Mehrpooya, and Erfan Ghavami Nezhad. 2018. "Latent and Sensible Heat Analysis

564   of PCM Incorporated in a Brick for Cold and Hot Climatic Conditions, Utilizing Computational Fluid

565   Dynamics." *Energy* 159: 160–71. https://doi.org/10.1016/j.energy.2018.06.074.

566   Ehms, José Henrique Nazzi, Rejane De Césaro Oliveski, Luiz Alberto Oliveira Rocha, Cesare Biserni, and

567   Massimo Garai. 2019. "Fixed Grid Numerical Models for Solidification and Melting of Phase Change

568   Materials (PCMs)." *Applied Sciences* 9: 4334. https://doi.org/10.3390/app9204334.

569   Hasnain, S M. 1998. "Review on Sustainable Thermal Energy Storage Technologies, Part I: Heat Storage

570   Materials and Techniques." *Energy Conversion and Management* 39 (11): 1127–38.

571   Ibrahim, Nasiru I., Fahad A. Al-Sulaiman, Saidur Rahman, Bekir S. Yilbas, and Ahmet Z. Sahin. 2017.

572   "Heat Transfer Enhancement of Phase Change Materials for Thermal Energy Storage Applications: A

573   Critical Review." *Renewable and Sustainable Energy Reviews* 74: 26–50.

574   https://doi.org/10.1016/j.rser.2017.01.169.

575 Jaguemont, Joris, Noshin Omar, Peter Van den Bossche, and Joeri Mierlo. 2018. "Phase-Change Materials

576   (PCM) for Automotive Applications: A Review." *Applied Thermal Engineering* 132: 308–20.

577   https://doi.org/10.1016/j.applthermaleng.2017.12.097.

578 Jamil, Nurfatihah, Jesbains Kaur, Ak. Pandey, Syed Shahabuddin, Samir Hassani, Rahman Saidur,

579   Roshafima Rasit Ali, Nor Azwadi Che Sidik, and Mohd Naim. 2019. "A Review on Nano Enhanced

580   Phase Change Materials: An Enhancement in Thermal Properties and Specific Heat Capacity."*Journal

581   of Advanced Research in Fluid Mechanics and Thermal Sciences* 57: 110-120.

582 Ji, Chenzhen, Zhen Qin, Swapnil Dubey, Fook Hoong Choo, and Fei Duan. 2018. "Simulation on PCM

583   Melting Enhancement with Double-Fin Length Arrangements in a Rectangular Enclosure Induced by

584   Natural Convection." *International Journal of Heat and Mass Transfer* 127: 255–65.

585   https://doi.org/10.1016/j.ijheatmasstransfer.2018.07.118.

586 Joshi, Varun, and Manish K. Rathod. 2019. "Constructal Enhancement of Thermal Transport in Latent Heat

587   Storage Systems Assisted with Fins." *International Journal of Thermal Sciences* 145 (November).

588   https://doi.org/10.1016/j.ijthermalsci.2019.105984.

589 Kalbasi, Rasool, and Mohammad Reza Salimpour. 2015. "Constructal Design of Horizontal Fins to Improve

590   the Performance of Phase Change Material Rectangular Enclosures." *Applied Thermal Engineering* 91:

591   234–44. https://doi.org/10.1016/j.applthermaleng.2015.08.024.

592 Kalnaes, Simen Edsjo, Bjorn Petter Jelle. 2015. "Phase change materials and products for building

593   applications: A state-of-the-art review and future research opportunities." *Energy and Buildings* 94:

594   150-176. https://dx.doi.org/10.1016/j.enbuild.2015.02.023.

595 Kamkari, Babak, and Hossein Shokouhmand. 2014. "Experimental Investigation of Phase Change Material

596   Melting in Rectangular Enclosures with Horizontal Partial Fins." *International Journal of Heat and

597   Mass Transfer* 78: 839–51. https://doi.org/10.1016/j.ijheatmasstransfer.2014.07.056.

598 Kazemi, M., M. J. Hosseini, A. A. Ranjbar, and R. Bahrampoury. 2018. "Improvement of Longitudinal Fins

599   Configuration in Latent Heat Storage Systems." *Renewable Energy* 116: 447–57.

600   https://doi.org/10.1016/j.renene.2017.10.006.

601 Khan, Mohammed Mumtaz A., R. Saidur, Fahad A. Al-Sulaiman. 2017. "A review for phase change

602   materials (PCMs) in solar absorption refrigeration systems." *Renewable and Sustainable Energy

603   Reviews* 76: 105-137. https://doi.org/10.1016/j.rser.2017.03.070.

604 Kok, Besir. 2020. "Examining Effects of Special Heat Transfer Fins Designed for the Melting Process of

605   PCM and Nano-PCM." *Applied Thermal Engineering* 170 (April).

606   https://doi.org/10.1016/j.applthermaleng.2020.114989.

607 Leducq, D., F. T. NDoye, G. Alvarez. 2015. "Phase change material for the thermal protection of ice cream

608   during storage and transportation." *International Journal of Refrigeration* 52: 133-139.

609   http://dx.doi.org/10.1016/j.ijrefrig.2014.08.012.

Mostafavi, Amirhossein, Mohammad Parhizi, and Ankur Jain. 2019. "Theoretical Modeling and
    Optimization of Fin-Based Enhancement of Heat Transfer into a Phase Change Material." *International
    Journal of Heat and Mass Transfer* 145 (December).
    https://doi.org/10.1016/j.ijheatmasstransfer.2019.118698.

Pielichowska, Kinga, and Krzysztof Pielichowski. 2014. "Phase Change Materials for Thermal Energy
    Storage." *Progress in Materials Science* 65: 67–123. https://doi.org/10.1016/j.pmatsci.2014.03.005.

Pizzolato, Alberto, Ashesh Sharma, Kurt Maute, Adriano Sciacovelli, and Vittorio Verda. 2017. "Design of
    Effective Fins for Fast PCM Melting and Solidification in Shell-and-Tube Latent Heat Thermal Energy
    Storage through Topology Optimization." *Applied Energy* 208 (October): 210–27.
    https://doi.org/10.1016/j.apenergy.2017.10.050.

Pu, Liang, Shengqi Zhang, Lingling Xu, and Yanzhong Li. 2020. "Thermal Performance Optimization and
    Evaluation of a Radial Finned Shell-and-Tube Latent Heat Thermal Energy Storage Unit." *Applied
    Thermal Engineering* 166 (November 2019): 114753.
    https://doi.org/10.1016/j.applthermaleng.2019.114753.

Reddy, K. S., Vijay Mudgal, and T. K. Mallick. 2018. "Review of Latent Heat Thermal Energy Storage for
    Improved Material Stability and Effective Load Management." *Journal of Energy Storage* 15: 205–27.
    https://doi.org/10.1016/j.est.2017.11.005.

Shokouhmand, Hossein, and Babak Kamkari. 2013. "Experimental Investigation on Melting Heat Transfer
    Characteristics of Lauric Acid in a Rectangular Thermal Storage Unit." *Experimental Thermal and
    Fluid Science* 50: 201–12. https://doi.org/10.1016/j.expthermflusci.2013.06.010.

Souayfane, Farah, Farouk Fardoun, Pascal-Henry Biwole. 2016. "Phase change materials (PCM) for cooling
    applications in buildings: A review."*Energy and Buildings* 129: 396-431.
    http://dx.doi.org/10.1016/j.enbuild.2016.04.006.

Sun, Kun, Huan Liu, Xiaodong Wang, and Dezhen Wu. 2019. "Innovative Design of Superhydrophobic
    Thermal Energy-Storage Materials by Microencapsulation of n-Docosane with Nanostructured
    ZnO/SiO2 Shell." *Applied Energy* 237 (January): 549–65.
    https://doi.org/10.1016/j.apenergy.2019.01.043.

Valeri, Daniella, and Antonio J.A. Meirelles. 1997. "Viscosities of Fatty Acids, Triglycerides, and Their
    Binary Mixtures." *JAOCS, Journal of the American Oil Chemists' Society* 74 (10): 1221–26.
    https://doi.org/10.1007/s11746-997-0048-6.

Voller, V. R., and C. Prakash. 1987. "A Fixed Grid Numerical Modelling Methodology for Convection-
    Diffusion Mushy Region Phase-Change Problems." *International Journal of Heat and Mass Transfer*
    30 (8): 1709–19. https://doi.org/10.1016/0017-9310(87)90317-6.

Wu, Shaofei, Ting Yan, Zihan Kuai, and Weiguo Pan. 2020. "Thermal Conductivity Enhancement on Phase
    Change Materials for Thermal Energy Storage: A Review." *Energy Storage Materials* 25 (September
    2019): 251–95. https://doi.org/10.1016/j.ensm.2019.10.010.

646   Zhang, Huili, Jan Baeyens, Gustavo Cáceres, Jan Degrève, and Yongqin Lv. 2016. "Thermal Energy
647   Storage: Recent Developments and Practical Aspects." *Progress in Energy and Combustion Science*
648   53: 1–40. https://doi.org/10.1016/j.pecs.2015.10.003.

649   Zhang, Xuelai, Xudong Chen, Zhong Han, and Weiwen Xu. 2016. "Study on Phase Change Interface for
650   Erythritol with Nano-Copper in Spherical Container during Heat Transport." *International Journal of*
651   *Heat and Mass Transfer* 92: 490–96. https://doi.org/10.1016/j.ijheatmasstransfer.2015.08.095.

652   Zhu, Na, Zhenjun Ma, and Shengwei Wang. 2009. "Dynamic Characteristics and Energy Performance of
653   Buildings Using Phase Change Materials: A Review." *Energy Conversion and Management* 50 (12):
654   3169–81. https://doi.org/10.1016/j.enconman.2009.08.019.
655
656